Turbulence during the reflection of internal gravity waves at critical and near-critical slopes

Vamsi K. Chalamalla[1]**, Bishakhdatta Gayen**[1]**, Alberto Scotti**[2]
and Sutanu Sarkar[1,†]

[1]Mechanical and Aerospace Engineering, University of California, San Diego, La Jolla, CA 92093, USA

[2]Department of Marine Sciences, University of North Carolina, Chapel Hill, NC 27599, USA

Direct numerical simulation is performed with a focus on the characterization of nonlinear dynamics during reflection of a plane internal wave at a sloping bottom. The effect of incoming wave amplitude is assessed by varying the incoming Froude number, Fr, and the effect of off-criticality is assessed by varying the slope angle in a range of near-critical values. At low Fr, the numerical results agree well with linear inviscid theory of near-critical internal wave reflection. With increasing Fr, the reflection process becomes nonlinear with the formation of higher harmonics and the initiation of fine-scale turbulence during the evolution of the reflected wave. Later in time, the wave response becomes quasi-steady with a systematic dependence of turbulence on the temporal and spatial phase. Convective instabilities are found to play a crucial role in the formation of turbulence during each cycle. The cycle evolution of flow statistics is studied in detail and qualitative differences between off-critical and critical reflection are identified. The parametric dependence of turbulence levels on Froude number and slope angle is calculated. Interestingly, at a given value of Fr, the turbulent kinetic energy (TKE) can be higher for somewhat off-critical reflection compared to exactly critical reflection. For a fixed slope angle, as the Froude number increases in the simulated cases, the fraction of the input wave energy converted into the turbulent kinetic energy and the fraction of the input wave power dissipated by turbulence also increase.

Key words: internal waves, stratified turbulence, turbulent flows

---

1. Introduction

Quantification of oceanic mixing rates is crucial for the correct modelling of Meridional Overturning Circulation (Park & Bryan 2000; Vallis 2000; Wunsch & Ferrari 2004). Interestingly, the latter is sensitive not only to the magnitude of mixing, but also to its spatial distribution (Saenko 2005). Several field measurements have been presented in recent years which reveal increased mixing and dissipation rates near the boundaries. High levels of dissipation (and by inference, mixing) in bottom layers that can extend to several hundred metres above the bottom are found near topographic

† Email address for correspondence: ssarkar@ucsd.edu

boundaries (Eriksen 1998; Munk & Wunsch 1998; Laurent & Garrett 2002; Moum *et al.* 2002; Nash *et al.* 2004; Aucan *et al.* 2006), often associated with tidal frequencies. The barotropic tidal velocity is mild and the barotropic tidal boundary layer is too thin to explain these observations. It is thought that internal tides (internal waves generated at bottom topography by the oscillatory tide) are responsible for the enhanced dissipation. This is due to the peculiar dispersion relationship satisfied by internal waves (Phillips 1977). It constrains the angle α between the horizontal direction and the group velocity vector to satisfy, in the non-rotating case,

$$\sin \alpha = \frac{\Omega}{N_\infty}, \tag{1.1}$$

where Ω is the frequency of the wave (conserved during reflection) and N_∞ the value of the Brünt–Väisälä frequency (buoyancy frequency, assumed constant). A similar relationship exists in the rotating case. As a consequence, when a plane wave reflects off a sloping bottom, the component of the wavenumber of the reflected wave in the direction normal to the group velocity increases by a factor $\sim |\alpha - \beta|^{-1}$, where β is the slope angle of the boundary. When β is close to α (the critical angle), this can lead to high levels of shear and increases the energy density of the reflected wave, leading to the well-known breakdown of the theory in the frequency domain when $\beta = \alpha$ (Dauxois & Young 1999; Scotti 2011). Whether coincidentally, or because of a feedback mechanism (Cacchione, Pratson & Ogston 2002), the slope β of most continental slopes is close to the critical angle for the semidiurnal internal tide. Thus, critical or near-critical reflection is a potentially widespread phenomenon that needs to be properly understood in order to quantify its contribution to the global mixing within the ocean. It is worth noting that critical slopes have also been implicated as hot spots of turbulence in generation regions (Gayen & Sarkar 2010, 2011*a*; Bluteau, Jones & Ivey 2011).

Theoretically, internal waves have been treated most frequently in the frequency domain (Wunsch 1968; Phillips 1977; Thorpe 1987; Tabaei, Akylas & Lamb 2005), but such an approach leads to divergent behaviour in the physical quantities at criticality. However, Dauxois & Young (1999) and recently Scotti (2011) have shown that in the time domain a laminar solution can be constructed even at criticality, neglecting nonlinear terms. It was used to infer the possible pathways for turbulence to develop. The solution obtained by Scotti (herein referred to as S11) shows that both shear and convective-driven instabilities can be found. The former are mostly found near the boundary. Since the S11 solution is inviscid, its validity in the immediate proximity of the boundary is questionable. However, convectively unstable regions are predicted in patches originating away from the boundary, reminiscent of what was observed in laboratory experiments (DeSilva, Imberger & Ivey 1997).

Two-dimensional numerical experiments were performed by Javam, Imberger & Armfield (1999) to study the nonlinear processes induced by internal wave reflection. Higher harmonics were observed near the boundary and attributed by the authors to nonlinear interactions between incident and reflected waves. Overturning was seen close to the wall at critical frequency and the region of overturning moved away from the wall as the off-criticality increased. Recently, two-dimensional numerical experiments as well as laboratory experiments were performed by Rodenborn *et al.* (2011) to study the reflection of internal wave beams at various slope angles and wave amplitudes. Except for very weak incoming waves, the highest amplitude of the reflected internal wave beam at the second harmonic frequency occurred when the

slope angle was significantly shallower than the critical angle. This study suggests that reflection at near-critical slopes may also play an important role in turbulence and mixing. A three-dimensional computational model for internal wave reflection was developed by Slinn & Riley (1998*a*) and numerical simulations (direct numerical (DNS) and large-eddy simulations (LES) using a hyperviscosity) were performed by Slinn & Riley (1998*b*) for cases with critical slope angle. Cyclical turbulence with periodic density overturns was found when the Reynolds number based on wavelength and peak velocity of the incident wave exceeded 1500. Examination of the local value of Richardson number suggested that both shear and convective instabilities could occur.

Previous studies have clearly shed some light on the nonlinear reflection processes that occur when the slope is critical. However, there seems to be no clarity regarding the mechanism of transition to turbulence, whether initiated by convective or shear instabilities. The importance of off-criticality is still obscure, i.e whether it is the critical reflection or near off-critical reflections which plays the major role in mixing over the slopes. Also, the effect of slope angle and incoming wave strength on the reflection process needs better understanding. In view of these outstanding questions, we have performed a DNS study where the slope angle is systematically changed for various incoming-wave Froude numbers and the numerical data are examined to identify the instabilities that lead to turbulence, to characterize the phasing of turbulence in the quasi-steady state, and to ascertain differences between critical and off-critical reflection as a function of incoming wave amplitude.

The paper is organized as follows: § 2 describes the formulation of the problem, and boundary and initial conditions. Section 3 presents results for laminar cases that are compared with analytical solutions. Section 4 discusses the mechanism and phasing of turbulence events. Sections 5 and 6 describe the parametric dependence of turbulent kinetic energy (TKE) and dissipation. The paper concludes with a summary of the results of the present numerical experiments.

2. Formulation of the problem

2.1. *Governing equations*

Direct numerical simulation is used to solve the Navier–Stokes equations, under the Boussinesq approximation in a non-rotating environment. The Navier–Stokes equations for dimensional variables (denoted by subscript *d*) are written as

$$\nabla \cdot \boldsymbol{u}_d = 0, \tag{2.1a}$$

$$\frac{\mathrm{D}\boldsymbol{u}_d}{\mathrm{D}t_d} = -\frac{1}{\rho_0}\nabla p_d^* - \frac{g\rho_d^*}{\rho_0}\hat{\boldsymbol{k}} + \nu\nabla^2\boldsymbol{u}_d, \tag{2.1b}$$

$$\frac{\mathrm{D}\rho_d}{\mathrm{D}t_d} = \kappa\nabla^2\rho_d. \tag{2.1c}$$

Here, p_d^* denotes deviation from the background hydrostatic pressure and ρ_d^* denotes the deviation from the linear background state, $\rho_d^b(z_d)$. The quantities u_d, v_d, w_d denote streamwise, spanwise and vertical velocity, respectively. The evolution equation for ρ_d^*, the deviation density, is written as

$$\frac{\mathrm{D}\rho_d^*}{\mathrm{D}t_d} = \kappa\nabla^2\rho_d^* - w_d\frac{\mathrm{d}\rho_d^b}{\mathrm{d}z_d}. \tag{2.2}$$

The dimensional parameters in the problem are the amplitude of the incident wave velocity in the x-direction U_0, frequency Ω, x-direction wavenumber k_d, background density gradient $\mathrm{d}\rho_d^b/\mathrm{d}z_d$, acceleration due to gravity g and the fluid properties: molecular viscosity, ν, thermal diffusivity, κ, reference density, ρ_0. The variables in the problem are non-dimensionalized as follows:

$$t = t_d \Omega, \, \boldsymbol{x} = (x, y, z) = \frac{(x_d, y_d, z_d)}{1/k}, \quad p^* = \frac{p_d^*}{\rho_0 U_0 \Omega / k_d}, \\ \boldsymbol{u} = (u, v, w) = \frac{(u_d, v_d, w_d)}{U_0}, \quad \rho^* = \frac{\rho_d^*}{\rho_0 U_0 \Omega / g}. \right\}$$ (2.3)

The non-dimensional parameters that govern the flow are Reynolds number Re, Froude number Fr, N_∞^2/Ω^2 and Prandtl number Pr.

The resulting non-dimensional form of the governing equations is:

$$\nabla \cdot \boldsymbol{u} = 0,$$ (2.4a)

$$\frac{\partial \boldsymbol{u}}{\partial t} + Fr(\boldsymbol{u} \cdot \nabla)\boldsymbol{u} = -\nabla p^* - \rho^* \boldsymbol{k} + \frac{Fr}{Re}\nabla^2 \boldsymbol{u},$$ (2.4b)

$$\frac{\partial \rho^*}{\partial t} + Fr(\boldsymbol{u} \cdot \nabla)\rho^* = FrRe^{-1}Pr^{-1}\nabla^2 \rho^* + \frac{N_\infty^2}{\Omega^2}w.$$ (2.4c)

The non-dimensional parameters are defined as follows:

$$Re = \frac{U_0}{\nu k_d}, \quad Fr = \frac{U_0 k_d}{\Omega}, \quad \frac{N_\infty^2}{\Omega^2} = -\frac{g}{\rho_0 \Omega^2}\frac{\mathrm{d}\rho_d^b}{\mathrm{d}z_d}, \quad Pr = \frac{\nu}{\kappa}.$$ (2.5)

The Froude number as defined here measures the distance of wave self-advection relative to the wavelength and thus the nonlinearity of the incoming wave. Note that $Fr/\sqrt{N_\infty^2/\Omega^2} = U_0 k_d/N_\infty$ can be taken as a measure of the nonlinearity of the highest-frequency internal wave in the system.

The dimensional form of the governing equations in the reference axis system $[x_s, y_s, z_s]$ rotated by an angle β in the x–z plane is given by

$$\nabla \cdot \boldsymbol{u}_s = 0,$$ (2.6a)

$$\frac{\mathrm{D}\boldsymbol{u}_s}{\mathrm{D}t} = -\frac{1}{\rho_0}\nabla p^* - \frac{g\rho^*}{\rho_0}(\sin\beta\boldsymbol{i} + \cos\beta\boldsymbol{k}) + \nu\nabla^2 \boldsymbol{u}_s,$$ (2.6b)

$$\frac{\mathrm{D}\rho^*}{\mathrm{D}t} = \kappa\nabla^2 \rho^* - \frac{\mathrm{d}\rho^b}{\mathrm{d}z}(u_s \sin\beta + w_s \cos\beta).$$ (2.6c)

Here, u_s, v_s, w_s are along-slope, spanwise and slope-normal velocities respectively in a rotated coordinate system. Subscript d for dimensional variables is dropped for convenience. Equations (2.6a)–(2.6c) will be solved numerically; details of the numerical method are discussed in the following section.

2.2. *Wave forcing*

Volumetric body forcing (Slinn & Riley 1998b) is employed to generate incident waves that propagate towards the slope from above and subsequently reflect as shown in figure 1. The cases to be considered are at critical slope angle and somewhat off-critical. Volume forcing has been implemented here by adding forcing functions $(F_u, F_w, -\mathrm{d}\rho^b/\mathrm{d}zF_\rho)$ to the right-hand side of the u_s, w_s and ρ equations in the rotated
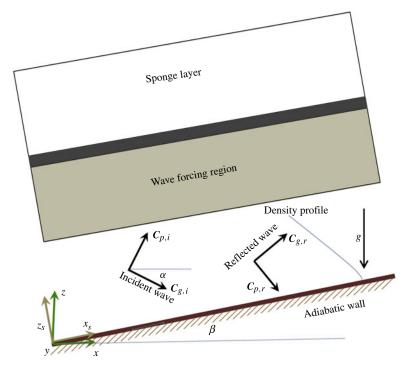
FIGURE 1. (Colour online) Schematic of the problem of internal wave reflection at a slope. $\boldsymbol{C}_g$ and $\boldsymbol{C}_p$ are group and phase velocity vectors respectively. The slope makes an angle β with respect to the horizontal and the angle that the phase lines make with the horizontal is denoted by α. The density profile shown is referenced to the slope normal axis z_s. The coordinate, z_s, is related to the vertical coordinate z by $z = x_s \sin\beta + z_s \cos\beta$.

coordinate system as follows:

$$F_u = -\frac{A_0 m_s}{k_s} F(z_s) \cos(k_s x_s + m_s z_s - \Omega t) - \frac{A_0}{k_s} F'(z_s) \sin(k_s x_s + m_s z_s - \Omega t), \quad (2.7a)$$

$$F_w = A_0 F(z_s) \cos(k_s x_s + m_s z_s - \Omega t), \quad (2.7b)$$

$$F_\rho = -\frac{A_0 \cos(\beta)}{\Omega} F(z_s) \sin(k_s x_s + m_s z_s - \Omega t) + \frac{A_0 m_s \sin(\beta)}{\Omega k_s} F(z_s)$$
$$\times \sin(k_s x_s + m_s z_s - \Omega t) - \frac{A_0 \sin(\beta)}{\Omega k_s} F'(z_s) \cos(k_s x_s + m_s z_s - \Omega t). \quad (2.7c)$$

Here, $F(z_s)$ is the localization function given by $F(z_s) = \exp[-b(z_s - z_{s0})^2]$, the parameter z_{s0} is the centre of the forcing region, $b = 50$ m^{-2}. Here, k_s and m_s are the slope-parallel and slope-normal wave number, respectively, while $F'(z_s)$ is the derivative of $F(z_s)$ w.r.t z_s. A_0 is chosen to impose a given value of Fr. At low Fr with domain height of 2 m, the forcing region is centred at $z_{s0} = 1.1$ m and is between $z_s = 0.85$ and 1.35 m. At high Fr with domain height of 4 m, the forcing region is centred at $z_{s0} = 1.8$ m and is between $z_s = 1.55$ and 2.05 m. In order to prevent the spurious accumulation of energy near the forcing region in the near-critical cases with higher Froude number ($Fr = 0.11$ and 0.148), a high-order filter is applied to the velocity field (u_s, v_s, w_s) in the slope-normal direction. Filtering is limited to a region between $z_s = 1.5$ and 2.5 m that is far away from the turbulent near-boundary region.

A fourth-order compact filter with the filter width parameter $\alpha = 0.48$ (Lele 1992) is chosen so that only the highest wavenumbers are affected.

2.3. *Boundary conditions*

No-slip boundary conditions have been imposed at the bottom boundary for u_s, v_s, w_s.

The total density can be written as summation of background density, and incident and reflected components of deviation densities:

$$\rho = \rho_0 - z_s \cos \beta - x_s \sin \beta + \rho^*. \qquad (2.8)$$

A zero-mass-flux boundary condition is imposed at the sloping bottom resulting in the density deviation at the sloping boundary given by

$$\frac{\partial \rho^*}{\partial z_s} = \cos \beta. \qquad (2.9)$$

2.4. *Numerical method*

The simulations use a mixed spectral/finite-difference algorithm. Derivatives in the streamwise and spanwise directions are treated with a pseudo-spectral method and derivatives in the vertical direction are computed with second-order finite differences. A staggered grid is used in the wall-normal direction. A low-storage third-order Runge–Kutta–Wray method is used for time stepping, and viscous terms are treated implicitly with the Crank–Nicolson method. The code has been parallelized using the message passing interface (MPI). Periodicity is imposed in the x_s and y_s directions. The top boundary is an artificial boundary corresponding to the truncation of the domain in the vertical direction. Rayleigh damping or a sponge layer is used to minimize spurious reflections from the artificial boundary into the computational domain. The velocity and scalar fields are relaxed towards the background state in the sponge region by adding damping functions $-\sigma(z_s)[(u_s, v_s, w_s)]$ and $-\sigma(z_s)[\rho^*]$ to the right-hand side of the momentum and scalar equations, respectively. The sponge region lies between $z_s = 1.5$ and 2 m in the low-Fr cases with domain height of 2 m, and between $z_s = 2.5$ and 4 m at the higher $Fr = 0.148$ with domain height of 4 m. The value of $\sigma(z_s)$ increases exponentially from zero at the bottom boundary of the sponge to a maximum value of $\sigma(z_s)\Delta t \sim O(0.1)$. The pressure boundary conditions are $p^* = 0$ at the bottom wall (due to the staggered grid) and $\partial p^*/\partial z_s = 0$ at the top of computational domain. Variable time stepping with a fixed CFL number of 1.2 is used. All the simulations are well resolved with $\Delta x^+ \leqslant 20$, $\Delta y^+ \leqslant 10$, $\Delta z^+ \leqslant 2$ in terms of the viscous wall unit ν/u_τ. Here, $u_\tau = \sqrt{\tau_w/\rho}$, with τ_w denoting the shear stress at the wall defined as follows:

$$\tau_w = \mu \sqrt{\left(\frac{\mathrm{d}u_s}{\mathrm{d}z_s}\right)^2_{z_s=0} + \left(\frac{\mathrm{d}v_s}{\mathrm{d}z_s}\right)^2_{z_s=0}}. \qquad (2.10)$$

In all the simulated cases, the wave has the same horizontal wavenumber $k = 3.84$ m^{-1}, frequency $\Omega = 0.15$ s^{-1} corresponding to a time period of $T = 41.9$ s, and internal wave angle $\alpha = 15°$. The background stratification is $N_\infty = 0.5795$ s^{-1}, dynamic viscosity is $\mu = 10^{-3}$ Pa s and kinematic viscosity is $\nu = 10^{-6}$ m^2 s^{-1}. The corresponding non-dimensional parameters are $N_\infty^2/\Omega^2 = 14.928$ and Prandtl number $Pr = 1.0$.

Three series of simulations are performed. Table 1 shows parameters for a series of simulations at a constant value of a near-critical slope angle ($\beta = 10°$), wave angle

Case	U_0 (m s^{-1})	Fr	Re	α (deg.)	β (deg.)	Remark
FR1	0	0	0	15	10	Laminar
FR2	1.0×10^{-4}	0.003	26	15	10	Laminar
FR3	1.1×10^{-3}	0.029	286	15	10	Laminar
FR4	2.8×10^{-3}	0.074	750	15	10	Turbulent
FR5	4.3×10^{-3}	0.110	1114	15	10	Turbulent
FR6	5.7×10^{-3}	0.148	1484	15	10	Turbulent

TABLE 1. Parameters of the first series of simulations to study the effect of Froude number, Fr, by varying the wave amplitude. The slope angle β is 5° smaller than the internal wave propagation angle of 15°. The along-slope domain size of $l_{xs} = 2\lambda_{xs} = 2$ m permits two wavelengths and the spanwise length is $l_{ys} = 0.25$ m. For cases FR1–FR4, the domain height is $l_{zs} = 2.0$ m and, for cases FR5 and FR6, $l_{zs} = 4.0$ m. Multiply Re by 2π to obtain Reynolds number based on horizontal wavelength, λ, instead of the horizontal wavenumber, k. In all these simulations, the ratio Fr/Re is kept constant at $\approx 10^{-4}$.

Case	$Fr = U_0 k / \Omega$	β (deg.)	Remark
FR4S15	0.074	15	Transition
FR4S10	0.074	10	Turbulent
FR4S5	0.074	5	Transition

TABLE 2. Series A with the amplitude of the incoming wave fixed at $Fr = 0.074$. The role of off-criticality is explored by changing the slope angle. The wave propagation angle is $\alpha = 15°$. FR4S10 has the Froude number of case FR4 (table 1) and a slope angle of 10°, similarly for other cases. The domain size is $l_{xs} = 2\lambda_{xs}$ m, $l_{ys} = 0.25$ m, $l_{zs} = 2.0$ m. The grid size is $N_x = 256$, $N_y = 64$, $N_z = 221$.

of $\alpha = 15°$, and six values of incoming Froude number, Fr. The set of simulations, series A with parameters listed in table 5, was performed to explore the effect of off-criticality at a fixed low value of $Fr = 0.074$ by changing the slope angle. Series B with parameters listed in table 3 is analogous to series A but at a higher $Fr = 0.148$.

2.5. *Turbulence diagnostics*

Any fluctuating quantity in the flow field is defined by subtracting the spanwise average from the instantaneous value:

$$A' = A - \langle A \rangle_y, \tag{2.11}$$

$$\langle A \rangle_y = \frac{1}{l_y} \int_0^{l_y} A \, dy. \tag{2.12}$$

Detailed analysis of the TKE budget is important to understanding the mechanisms underlying the phasing of turbulence. The evolution of TKE is governed by the following equation:

$$\frac{dK}{dt} = P - \epsilon + B - \frac{\partial T_i'}{\partial x_j}, \tag{2.13}$$

where $K = \langle u_i' u_i' \rangle_y / 2$, $P = -\langle u_i' u_j' \rangle_y \langle S_{ij} \rangle_y$, $\epsilon = \nu \langle (\partial u_i'/\partial x_j) \partial u_i'/\partial x_j \rangle_y$, $B = g_i/\rho_0 \langle \rho^{*'} u_i' \rangle_y = -g/\rho_0 \langle \rho^{*'} w' \rangle_y$, $T_i' = 1/\rho_0 \langle p^{*'} u_j' \rangle_y - 2\nu \langle u_i' s_{ij}' \rangle_y + \langle u_i' u_i' u_j' \rangle_y / 2$. Here, K

Case	$Fr = U_0 k/\Omega$	β (deg.)	Remark
FR6S15	0.148	15	Turbulent
FR6S10	0.148	10	Turbulent
FR6S5	0.148	5	Turbulent

TABLE 3. Series B: as Series A but with the amplitude of the incoming wave fixed at $Fr = 0.148$. FR6S10 has the Froude number of case FR6 (table 1) and slope angle of 10°, similarly for other cases. The domain size is $l_{xs} = 2\lambda_{xs}$ m, $l_{ys} = 0.25$ m, $l_{zs} = 4.0$ m. The grid size is $N_x = 512$, $N_y = 128$, $N_z = 449$.

denotes turbulent kinetic energy, P is production, ϵ is turbulent dissipation rate, B is buoyancy flux with w' denoting the vertical velocity, $\partial T_i'/\partial x_j$ is the transport of turbulent kinetic energy with $s_{ij}' = (\partial u_i'/\partial x_j + \partial u_j'/\partial x_i)/2$.

Averaging over the slope-normal coordinate and over several cycles is employed to quantify turbulent statistics used to compare results at different Fr and slope angles. These averages are calculated as follows:

$$\langle A \rangle_{zt} = \frac{1}{z_1 t_1} \int_0^{z_1} \int_{t_1}^{t_2} A \, dt \, dz_s, \qquad (2.14)$$

where $z_1 = 0.25$ m, and t_1 and t_2 are chosen such that the averaging includes a minimum of four cycles in the quasi-steady state.

3. Laminar regime

The wave amplitude intensifies during reflection from a near-critical slope. However, when the incoming wave amplitude is small and the corresponding value of $Fr \ll 1$, the flow field associated with the reflected wave remains laminar. The effect of Fr in the laminar flow regime is discussed here.

3.1. *Velocity field*

Figure 2 shows contour plots of the along-slope instantaneous velocity field for cases FR1, FR2 and FR3 of table 1. Figure 2(a) corresponds to $Fr = 0$ with no forcing. The zero-mass-flux boundary condition at the inclined wall creates a slope-wise density gradient resulting in a thin boundary layer (Phillips 1970; Wunsch 1970) with a steady upslope flow, $u_s(z_s)$, that is established by a balance between viscous and buoyancy forces. The Phillips–Wunsch solution is realized in the absence of wave forcing as illustrated by figure 2(a). Figure 2(b,c) shows a reflected wave of along-slope wavelength 1 m that propagates at 15° angle to the horizontal corresponding to an angle of 5° relative to the boundary. With increasing wave forcing, the unidirectional boundary velocity field of the Phillips–Wunsch solution is dominated by the oscillatory wave response.

Numerical results for case FR3 are compared with the analytical solution obtained using linear inviscid theory by S11. Figure 3(a–c) shows the profiles of along-slope velocity. As time progresses, the velocity intensifies until it reaches a steady state after approximately five cycles. The vertical wavelength of the velocity decreases during the transient, as can be observed from the shortening distance between successive zero-velocity points in figure 3. Numerical results and the analytical solution are in good quantitative agreement in the region outside the boundary layer. Within the boundary layer, since viscous effects are prominent, the inviscid analytical solution deviates from
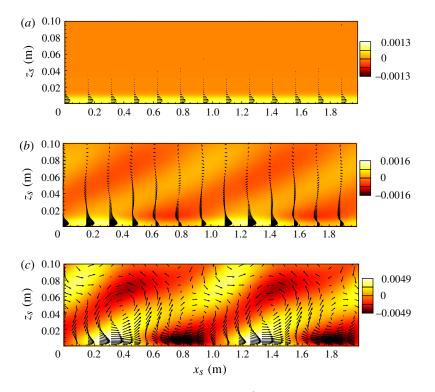
FIGURE 2. (Colour online) Contour plots of u_s (m s^{-1}) in the x_s–z_s plane at quasi-steady state for a constant slope angle ($\beta = 10°$) and different wave amplitudes: (*a*) no wave, $Fr = 0$, (*b*) $Fr = 0.0028$, (*c*) $Fr = 0.029$. Velocity vectors are also shown. Note that the z_s-axis corresponds to a smaller distance relative to the x_s-axis. The ratio Fr/Re is constant ($\approx 10^{-4}$) in all these cases, even when there is no wave (i.e. $Fr = 0$).

the DNS. In the inviscid analytical solution, the maximum along-slope velocity is at the bottom boundary, whereas it is maximum away from the wall in the DNS.

3.2. *Frequency spectra*

The distribution of energy among different frequencies is discussed in this section. Figure 4 shows the power spectrum of along-slope and slope-normal velocity for case FR3, a case with off-criticality of 5° and $Fr = 0.029$, at two locations. The spectra are evaluated over a period of six cycles. The spectra exhibit discrete frequencies in the form of multiples of the forcing harmonic ($n\Omega, n \in N$). These peaks carry a substantial fraction of the energy at $z_s = 0.17$ m. There are also local peaks at subharmonic frequencies of approximately, 0.3Ω and 0.7Ω.

To compare the spectra in case FR3 with 5° off-criticality with those in the case of critical slope, another simulation is done at an exactly critical slope angle and the results shown in figure 5. The spectra do not exhibit qualitative changes. One difference is that the spectrum of vertical velocity drops rapidly for $\omega > N_\infty$ in the near-critical case but, when the slope angle is critical, the spectra show some discrete peaks for $\omega > N_\infty$, that may correspond to forced waves generated and trapped in the near-boundary region.
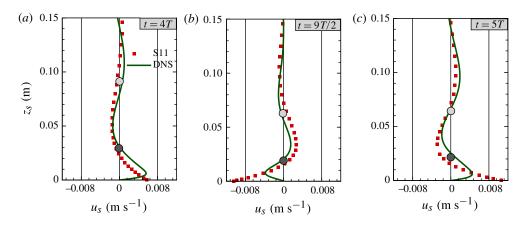
FIGURE 3. (Colour online) Profiles of along-slope reflected velocity component u_s as a function of wall-normal distance taken at $x_s = 1$ m for case FR3 at different time instances with a time gap of half a wave period. Corresponding profiles of theoretical solution by S11 are also shown in the figure (squares).
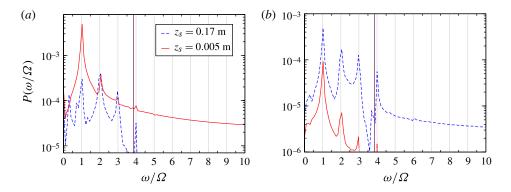

FIGURE 4. (Colour online) Off-critical case FR3 at $Fr = 0.029$ and slope angle of $10°$: power spectra of (*a*) along-slope velocity, and (*b*) slope-normal velocity, at two different heights $z_s = 0.005$ m and $z_s = 0.17$ m. The solid vertical line represents the frequency when $\omega = N_\infty$.

4. Turbulent regime

At sufficiently high values of incoming Froude number, the energy density in the reflected wave field is found to be large enough for stratified, phase-dependent turbulence to develop when the slope is either critical or somewhat off-critical. The inviscid, linear analysis of S11 concluded that, during the transient evolution of a near-critical reflected wave, unstable regions could occur and the present results are in agreement with that conclusion. DNS allows us to go beyond theory by making precise the mechanism of transition to turbulence during near-critical reflection as will be shown in §4.1 and quantifying the role of turbulence during the flow evolution. After the transient buildup of turbulence, the flow statistics reach an approximately quasi-steady dependence on wave phase. The phasing of turbulence during this quasi-steady state is found to have qualitative differences between critical and near-critical cases as described in §4.2.
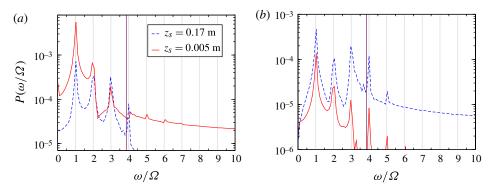
FIGURE 5. (Colour online) Critical case with $Fr = 0.029$ and slope angle of $15°$: power spectra of (*a*) along-slope velocity, and (*b*) slope-normal velocity, at two different heights $z_s = 0.005$ m and $z_s = 0.17$ m. The solid vertical line represents the frequency when $\omega = N_\infty$.

4.1. *The development of turbulence in near-critical cases*

During the transient evolution of the reflected wave, the fluid velocity increases and, correspondingly, the density deviation from the background increases. Since the near-bottom vertical wavelength also decreases, the isopycnals steepen leading to the possibility of wave breaking and turbulence. The simulations show wave breaking within one wavelength from the boundary. Figures 6(*a*) and 6(*b*) show contour plots of along slope-velocity and turbulent kinetic energy for case FR4S10 at time $t = 10T$. The velocity contours in figure 6(*a*) show the spatially periodic field corresponding to an internal wave as well as the velocity intensification (approximately 5 times that of the incoming wave) expected for near-critical reflection. The TKE field in figure 6(*b*) shows two locations of turbulence within a span of a single along-slope wavelength. These two turbulence patches, one close to the wall and another away from the wall, appear periodically during a cycle at any given streamwise coordinate. After the initial transient, the amplitude of the oscillatory TKE in these patches remains approximately constant corresponding to a quasi-steady state. Figure 6(*c*,*d*) shows vertical density profiles at locations 1 and 2 indicated in figure 6(*a*). The grey shaded regions in figures 6(*c*) and figure 6(*d*) are convectively unstable regions that correspond to turbulence locations near the wall and further away from the wall, respectively.

We now move to the development of turbulence in case FR6S10 with the same value of off-criticality, $5°$, as case FR4S10, but with a higher incoming wave amplitude corresponding to $Fr = 0.148$. Figure 7 shows contours of turbulent statistics in case FR6S10 at three time instances. Figure 7(*a–d*), comprising column 1, shows the onset of turbulence near the wall. Figure 7(*e–h*) corresponds to a later time when another patch of turbulence develops away from the wall. Figure 7(*i–l*) corresponds to the fully developed, quasi-steady state. At early time, $t = 4.8T$, there is a single patch of turbulence near the boundary, denoted by 1 in figure 7(*a*). At intermediate time, $t = 5.5T$, the near-wall patch 1 has strengthened and grown spatially. There is also an additional patch of turbulence detached from the boundary, denoted by 2 in figure 7(*e*). At time, $t = 7.7T$, the detached patch 2 is stronger in amplitude and also spatially larger (figure 7*i*). Examination of the isopycnals in front of the near-wall turbulence patch shows the presence of a thermal front with high streamwise temperature (density) variation. This front is found to propagate upslope as observed in previous laboratory experiments, e.g. Ivey & Nokes (1989), Thorpe (1992). The second row (figure 7*b*,*f*,*j*) shows positive buoyancy flux, associated with convective
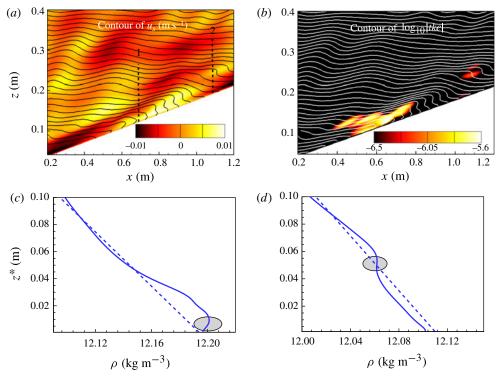
FIGURE 6. (Colour online) The development of intensified velocity and patches of turbulence during near-critical reflection is illustrated by spatial x–z cuts at $t = 10T$ for case FR4S10 with $Fr = 0.074$ and off criticality of $5°$: (*a*) contours of along-slope velocity, (*b*) contours of turbulent kinetic energy. Half the streamwise domain size, corresponding to a single wavelength, is shown. Convectively unstable regions (shaded ellipses) are shown by profiles of density as a function of height from the bottom at (*c*) location 1 and (*d*) location 2, indicated by dotted lines in (*a*).

instability, at all locations with enhanced TKE, while positive values of production are also seen in the third row (figure 7*c,g,k*). Noteworthy is the behaviour at quasi-steady state (column 3, figure 7*i–l*) where the correspondence of the detached large patch 2 of TKE to a similar large patch of positive buoyancy is clear. High dissipation is seen at all locations with enhanced TKE (figure 7*d,h,l*).

The analytical solution derived by S11 was evaluated for case FR6S10; a statically unstable region develops initially at the wall at a time that is earlier than in the DNS (where the first turbulence patch is observed at 4.8T), during flow reversal from downslope to upslope. Owing to the absence of the viscous boundary layer in the analytical solution, the statically unstable region during the other flow reversal event from upslope to downslope that was seen in the DNS is absent. At later time, a statically unstable region develops away from the wall and merges with the initial region so the region that could potentially break in the analytical solution to give turbulence is large. However, in the DNS, turbulence is found only in the region between the solid boundary and the first zero-crossing of the horizontal velocity. Evidently, in the simulations, turbulent mixing of the density and turbulent dissipation of momentum both change the isopycnal distribution above the first zero-crossing to prevent the internal wave from breaking into turbulence.
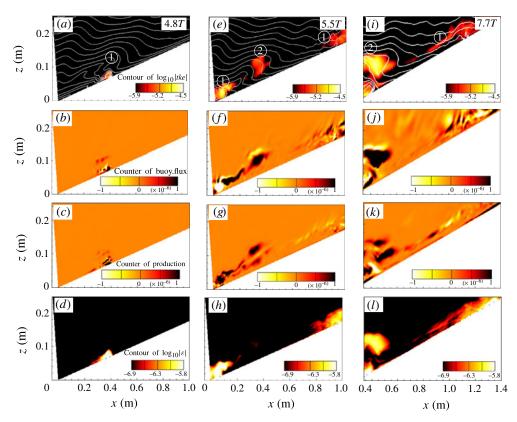
FIGURE 7. Turbulence statistics in an x–z plane are shown for case FR6S10 with $Fr = 0.148$ and near-critical slope angle of $10°$. Half the streamwise domain corresponding to a single wavelength is shown. Column 1 (a–d) corresponds to at an early time of $t = 4.8T$, column 2 (e–h) to a later time of $t = 5.5T$, and column 3 (i–l) to $t = 7.7T$ close to the quasi-steady state. Rows from top to bottom show contours of TKE (log scale), buoyancy flux, turbulent production and turbulent dissipation rate (log scale).

The TKE level increases with increasing wave amplitude. More interestingly, the spatial distribution of turbulence also depends on the incoming wave amplitude. At low $Fr = 0.074$, the patch near the boundary has higher TKE compared to the patch detached from the boundary as was noted earlier in figure 6(b). In contrast, for case FR6S10 with higher $Fr = 0.148$, TKE in the patch away from the wall is almost of the same magnitude as that in the patch near the wall. This is because, away from the boundary, the increase in the magnitude of density deviation caused by the higher wave amplitude of case FR6S10 is able to cause a thicker region of unstable density leading to a larger positive buoyancy flux and more intense turbulence. In contrast, the wall boundary condition limits the thickness of the overturning region that develops adjacent to the bottom boundary.

4.2. *Comparison of turbulence between critical and near-critical cases*

The nonlinear response differs qualitatively between critical and near-critical slopes. For instance, at low $Fr = 0.074$, there is little turbulence during critical reflection while the case with $5°$ off-criticality has substantial TKE and turbulent dissipation. Qualitative differences in near-bottom turbulence are discussed in this section by
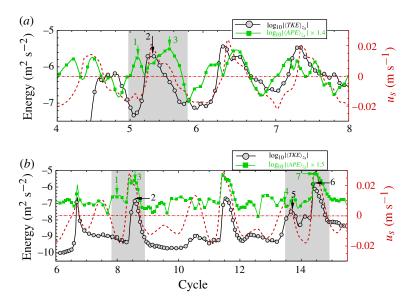
FIGURE 8. (Colour online) Time evolution of turbulent kinetic energy and available potential energy, averaged in the slope-normal direction, and measured at mid-slope comparing critical and near-critical cases: (*a*) critical slope angle $\beta = 15°$ (*b*) near-critical slope angle $\beta = 5°$ The dashed curve represents along-slope velocity. Both cases have wave angle of $\alpha = 15°$ and $Fr = 0.148$.

comparing cases FR6S15 (critical) and FR6S5 (10° off-criticality). Both cases have $Fr = 0.148$, wave propagation angle of 15°, and develop substantial levels of turbulence.

We now turn to the temporal phasing of turbulence. The time evolution of turbulent kinetic energy along with available potential energy, APE $= g^2\rho^{*2}/(2\rho_0^2 N_\infty^2)$ with ρ^* denoting the deviation from the background density, is shown for critical and near-critical slope reflection in figure 8. Both quantities are averaged over the slope-normal coordinate, $0 < z_s < 0.25$ m. The slope-wise velocity is also plotted to show the relative phases of peak TKE and APE. In the critical case, turbulence is initiated at cycle 4.5 as shown in figure 8(*a*). A peak in APE occurs twice in each cycle shortly prior to the zero-velocity point as shown by downward pointing arrows 1 and 3. The TKE increases when the APE is maximum (arrow 1) and it peaks as marked by arrow 2 before the upslope velocity reaches its maximum value. However, no peak of TKE is found after the peak APE (arrow 3) during the flow reversal from upslope to downslope motion.

The phasing of turbulence during near-critical reflection is shown in figure 8(*b*) and is now compared with the critical case. The important difference is that the TKE peaks skip cycles in contrast to the critical case where there is one TKE peak every cycle. During near-critical reflection, the first peak in TKE is found at $t = 6.5T$ as shown in figure 8(*b*). The next peak of TKE at approximately $t = 8.5T$, see arrow 2, occurs after two cycles during transition from up- to downslope flow and a peak in APE. During this cycle, there is a single peak of TKE with shear production playing an important role aided by the convective instability that occurs during flow reversal from upslope to downslope flow. The next peak of TKE occurs after three cycles at approximately $t = 11.5T$. Later, during cycle 14, there are two peaks in TKE: peak 5 occurs at a
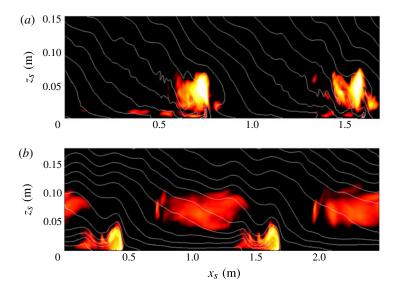
FIGURE 9. Spatial contours of turbulent kinetic energy at a quasi-steady state: (*a*) case FR6S15, with critical slope angle $\beta = 15°$ and $Fr = 0.148$, is shown at $t = 9.1T$; (*b*) case FR6S5 with near-critical slope angle, $\beta = 5°$ and $Fr = 0.148$, is shown at $t = 20.8T$.

similar downslope flow phase as the earlier peaks while the second peak (arrow 6) occurs shortly after flow reversal from downslope to upslope motion when there is a peak in APE (arrow 7). The different phasing of TKE in the near-critical case occurs because the interaction between the incident and reflected waves becomes important in this situation. Owing to this interaction, the wave field gets weaker periodically as evident from the small velocity peaks and little turbulence between cycles 9–11 in figure 8(*b*). Mean flows with little temporal variability are found during this quiescent period with little turbulence when the near-boundary wave field is weak. However, there is strong down- and upslope flow every three cycles (for example at $t = 8$–$8.5T$, 11–$11.5T$ and 14–$14.5T$) and correspondingly strong turbulence bursts during these periods.

Figure 9 shows a comparison of TKE contours during times with turbulence after a quasi-steady state has been reached. Critical slope reflection results in one turbulence burst every wavelength and the burst occurs close to the wall as shown in figure 9(*a*). Near-critical slope reflection results in two distinct patches of turbulence in a wavelength. The patch closer to the wall in figure 9(*b*) occurs during the transition from up- to downslope flow and the second patch that is detached from the wall occurs during the transition from down- to upslope flow.

Figure 10 shows the time evolution of production, dissipation and buoyancy flux averaged in the slope-normal direction for critical and near-critical slope angles. The difference observed between the critical and near-critical slope cases is that, for critical slope reflection, the peak of buoyancy flux is dominant when compared with the peak of turbulent production, whereas during near-critical slope reflection, both buoyancy flux and production are significant contributors to the increase in the turbulent kinetic energy. Figure 10(*a*), corresponding to the critical slope case, exhibits a positive peak in the averaged buoyancy flux at $8.2T$ when the near-bottom flow reverses from down- to upslope flow. There is some inter-cycle variability: the magnitude
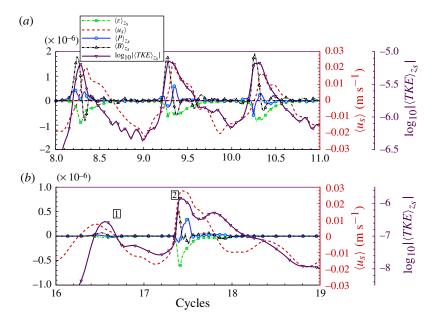
FIGURE 10. (Colour online) Comparison of terms in the TKE budget between critical and near-critical cases. Time evolution of production, dissipation and buoyancy flux averaged along the slope-normal direction at mid-slope. The dashed line is the along-slope velocity (averaged over 10 points near the maximum velocity location): (*a*) case FR6S15 with critical slope angle $\beta = 15°$ and $Fr = 0.148$; (*b*) case FR6S5 with near-critical slope angle, $\beta = 5°$ and $Fr = 0.148$.

of the buoyancy flux peak changes during the subsequent cycles (not shown here). Negative production, which is unusual in turbulent flows, is seen after the positive peak in buoyancy flux. The mechanism of the negative production in the context of internal tide generation has been shown by Gayen & Sarkar (2011*b*) to be related to shear acting on turbulence structures initiated by buoyancy, a mechanism that is also operative here. For near-critical slope reflection with off-criticality 10°, a period with turbulence peaks is shown in figure 10(*b*). The primary peak, marked 2, is associated with both positive buoyancy flux and shear production. There is an auxiliary peak marked 1 which occurs because of turbulence advection.

5. Mean kinetic energy

Turbulent dynamics has been discussed extensively in the previous section. The impact of turbulence on the mean flow is discussed in this section by making use of the mean kinetic energy equation.

The mean kinetic energy MKE $= (\langle u_i \rangle_y \langle u_i \rangle_y)/2$ evolves as

$$\frac{\partial (MKE)}{\partial t} + \langle u_j \rangle_y \frac{\partial (MKE)}{\partial x_j} = -P - \bar{\epsilon} + \bar{B} - \frac{\partial T_i}{\partial x_i}, \tag{5.1}$$

where $P = -\langle u_i' u_j' \rangle_y \langle S_{ij} \rangle_y$, $\bar{\epsilon} = \nu (\partial \langle u_i \rangle_y / \partial x_j)(\partial \langle u_i \rangle_y / \partial x_j)$, $\bar{B} = -g/\rho_0 \langle \rho^* \rangle_y \langle w \rangle_y$, $T_i = \langle p^*/\rho_0 \rangle_y \langle u_j \rangle_y - 2\nu \langle u_i \rangle_y S_{ij} + \langle u_i' u_j' \rangle_y \langle u_i \rangle_y$. Here P is production, $\bar{\epsilon}$ is the viscous dissipation rate of the mean velocity, $\bar{B}$ is the mean buoyancy flux with $\langle w \rangle_y$ denoting the mean vertical velocity, $\partial T_i / \partial x_i$ is the transport of mean kinetic energy with

	$\mathbb{P}/\mathbb{I}$	$\mathbb{D}/\mathbb{I}$	$-\mathbb{B}/\mathbb{I}$	$\mathbb{A}/\mathbb{I}$
FR6S15	0.06	0.51	0.42	0.005
FR6S5	0.035	0.44	0.48	0.04
FR4S10	0.03	0.51	0.42	0.03

TABLE 4. Ratio of integrated production, mean dissipation, mean buoyancy to the input energy flux, $\mathbb{I}$. The energy input is transferred to turbulent kinetic energy through $\mathbb{P}$, to mean potential energy through $-\mathbb{B}$, and dissipated by viscosity through $\mathbb{D}$, and the remaining energy represented by $\mathbb{A}$ is the flux advected out of the domain.

$S_{ij} = (\partial\langle u_i\rangle_y/\partial x_j + \partial\langle u_j\rangle_y/\partial x_i)/2$. The above equation is integrated in the slope-normal direction and time, e.g. the integrated advection is

$$\langle A\rangle_{zt} = \int_0^{z_1} \int_{t_1}^{t_2} A \, \mathrm{d}t \, \mathrm{d}z_s, \qquad (5.2)$$

where $z_1 = 1.5$ m, t_1 and t_2 are chosen such that at least four wave periods are included in the quasi-steady state.

Let the integrated unsteady (or tendency) term in (5.1) be denoted by $\mathbb{U}$, the advection term by $\mathbb{A}$, the transport term by $\mathbb{T}$, the production term by $\mathbb{P}$, the dissipation term by $\mathbb{D}$, and the buoyancy term by $\mathbb{B}$. After the reflected wave is established, the integrated values of advection and tendency are found to be approximately zero. Among the transport terms, the dominant contributor is the velocity–pressure correlation (internal wave flux). The value of the internal wave flux at $z_s = 1.5$ m is considered to be the input energy flux, $\mathbb{I}$, to the system that drives the near-boundary flow. The input, $\mathbb{I}$, is as follows:

$$\mathbb{I} = \int_0^{l_x} [\langle p^*\rangle \langle w_s\rangle]_{z_s=1.5} \, \mathrm{d}x_s. \qquad (5.3)$$

It is accessible for conversion to mean buoyancy, conversion to turbulence through production, and destruction through viscous effects. The production term, $\mathbb{P}$, is usually positive resulting in the gain of turbulent kinetic energy at the expense of a loss of mean kinetic energy. The mean buoyancy term is the work done by gravity on the mean vertical motion. A negative mean buoyancy term indicates a transfer to mean potential energy. The input flux, $\mathbb{I}$, computed at $z_s = 1.5$ has two components: (i) the wave field generated at the forcing region that travels towards the boundary, and (ii) the reflected wave field. The contribution of the reflected wave can be estimated by calculating the wave flux in a section above the wave forcing region and below the sponge region. It negligibly small in the exactly critical case FR6S15. However, in off-critical case FR6S5, since the reflected waves move away from the boundary, the radiated flux is significant ($\approx 10\%$ of the total incoming flux).

Three different cases (FR6S15, FR6S5, FR4S10) are examined to assess the role of the different terms in the mean kinetic energy equation. Table 4 lists various terms in the mean kinetic energy equation. The mean dissipation, $\mathbb{D}$, and the transfer to mean potential energy through $\mathbb{B}$ balance the input wave flux. For critical reflection, 89 % of the total mean dissipation occurs in the boundary region, i.e. $0 < z_s < 0.15$ m, and the remainder occurs outside the boundary layer. For the off-critical case FR6S5, 82 % of the total mean dissipation occurs in the boundary region. Mean dissipation is high in all the cases because of the relatively weak incident wave and low value
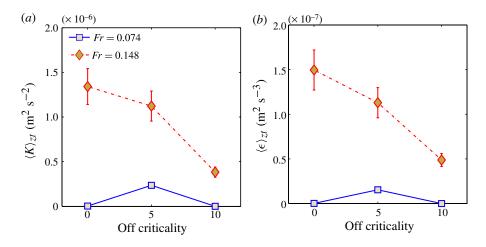
FIGURE 11. (Colour online) Cycle-averaged turbulent statistics at a mid-slope location and spatially averaged over a 0.25 m high boundary region are plotted as a function of off-criticality (degrees) in slope angle: (*a*) turbulent kinetic energy; (*b*) turbulent dissipation rate. The $\langle K \rangle_{zt}$ and $\langle \epsilon \rangle_{zt}$ values at $Fr = 0.074$ are *multiplied by a factor of* 2 so that the results can be shown in the same figure.

	Off-criticality (deg.)	0	5	10
$\tau_{w,avg}$	$Fr = 0.148$	0.1815	0.1406	0.1325

TABLE 5. Wall shear stress normalized with incoming wave along-slope amplitude, averaged over 10 cycles at a mid-slope location for different values of the off-criticality and $Fr = 0.148$.

of the Stokes Reynolds number, $Re_s = U_0 \delta_s / \nu$, where $\delta_s = \sqrt{2\nu/\Omega}$ is the Stokes boundary layer thickness: $Re_s = 20.8$ for cases FR6S15, FR6S5 and $Re_s = 10.22$ for case FR4S10. We emphasize that a typical Stokes boundary layer on a non-sloping bottom is laminar at these values of Re_s. It is the phenomenon of wave intensification and breaking associated with critical slope dynamics that results in turbulence in the present simulations, albeit at a Reynolds number much lower than in the ocean.

6. Parametric dependence of turbulence statistics

DNS results at various Froude numbers for every slope angle considered in our simulations are collected to characterize the TKE dependence on Froude number and off-criticality.

Figure 11 shows averaged turbulent kinetic energy, $\langle K \rangle_{zt}$, and averaged turbulent dissipation rate, $\langle \epsilon \rangle_{zt}$, at $Fr = 0.074$ and 0.148 as a function of off-criticality defined as the difference between internal wave angle ($\alpha = 15°$) and the slope angle (β) of the case in question. Thus, off-criticality of 0° corresponds to an exactly critical slope, while 10° off-criticality corresponds to a slope angle of 5°. At a low $Fr = 0.074$, the critical case is not turbulent, and the values of $\langle K \rangle_{zt}$ and $\langle \epsilon \rangle_{zt}$ are maximum when the off-criticality angle is 5° and then they drop. For the larger incoming wave amplitude

of the $Fr = 0.148$ series of simulations, $\langle K \rangle_{zt}$ and $\langle \epsilon \rangle_{zt}$ are maximum at critical slope reflection and then decrease monotonically as the off-criticality increases.

Table 5 shows the wall shear stress (normalized with ρU^2, where U is the amplitude of the incoming wave velocity in the along-slope direction), averaged over 10 cycles, recorded at mid-slope. The wall shear decreases with increasing off-criticality due to an increase in vertical length scale of the region of bottom turbulence.

Normalized values of turbulent statistics are defined as follows,

$$\mathcal{K} = \frac{2\langle K \rangle_{zt}}{U_0^2 + W_0^2}, \quad \mathcal{D} = \frac{2\langle \epsilon \rangle_{zt}}{\Omega\,(U_0^2 + W_0^2)}, \tag{6.1a}$$

$$\mathcal{B} = \frac{2\langle B \rangle_{zt}}{\Omega\,(U_0^2 + W_0^2)}, \quad \mathcal{P} = \frac{2\langle P \rangle_{zt}}{\Omega\,(U_0^2 + W_0^2)}. \tag{6.1b}$$

For a near-critical slope angle, $\beta = 10°$, the effect of Fr on various turbulent statistics is assessed. Figure 12(a) shows averaged turbulent kinetic energy, $\langle K \rangle_{zt}$, and figure 12(b) shows normalized turbulent kinetic energy, plotted as a function of Froude number. Similarly, figures 12(c) and 12(d) show averaged and normalized values of terms in the TKE balance: dissipation, buoyancy flux and production, respectively. A rapid increase in averaged turbulent kinetic energy is found with increasing Fr. Upon normalization using the incoming wave amplitude, a natural velocity scale for the problem, the turbulent kinetic energy does not increase at the highest value of Fr. Terms on the right-hand side of the TKE equation, such as turbulent dissipation rate, also rapidly increase with increasing Fr. Guided by the finding here that turbulence occurs during only a fraction of the cycle and that this fraction eventually shows little dependence on the incoming wave amplitude, we take the scaling of the terms in the TKE transport equation to be $\Omega(U_0^2 + W_0^2)$. Figure 12(d) shows that this normalization is able to substantially reduce the variation between cases at high Fr. An alternative normalization, based on $(U_0^2 + W_0^2)^{3/2}/\lambda$, was ruled out because it led to a systematic decrease with increasing Fr in the high-Fr regime.

7. Conclusions

The dynamics of internal waves reflected from a slope is examined as a function of incoming wave amplitude, measured by the wave Froude number, Fr, and the deviation of the slope angle, β, from the wave propagation angle, α. The choice of laboratory scale dimensions, e.g. the wave has a horizontal wavelength of $\lambda = 1.636$ m and a frequency of $\Omega = 0.15$ s^{-1}, allows the DNS approach that resolves turbulence, including the turbulent dissipation rate, without any additional models.

The effect of Fr at a near-critical slope angle is assessed. At zero Fr (no incoming wave), the numerical solution corresponds to a steady upslope streaming flow (Phillips 1970; Wunsch 1970) with a balance between buoyancy and viscous drag. Near-critical reflection with an off-criticality angle ($\alpha - \beta$) of 5° was examined for incoming waves with $0 < Fr < 0.148$. At low Fr, the internal wave response remains laminar. However, higher temporal frequencies, subharmonics and inter-harmonics are generated. During the initial transient, the near-bottom amplitude of the reflected wave increases and the near-bottom vertical wavelength decreases. The numerical solution in the laminar, low-Fr cases agrees well with the analytical, inviscid solution derived by Scotti (2011) for critical and near-critical reflection except at the wall where there is a viscous boundary layer in the DNS. At a sufficiently high value of incoming wave amplitude (Fr), there is transition to turbulence.
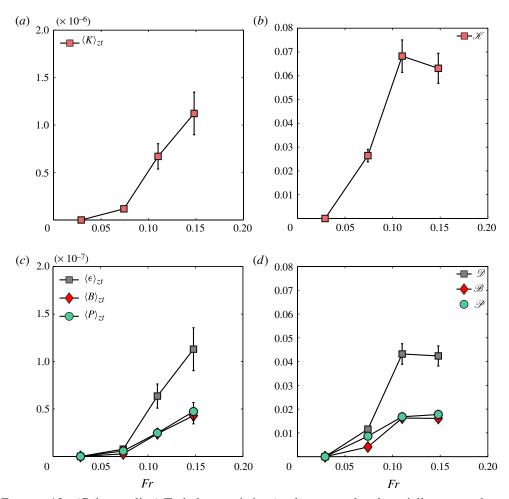
FIGURE 12. (Colour online) Turbulent statistics (cycle-averaged and spatially averaged over a 0.25 high boundary region at mid-slope) as a function of Froude number for a slope angle $\beta = 10°$: (*a*) averaged kinetic energy; (*b*) normalized kinetic energy; (*c*) averaged dissipation, buoyancy flux and production; (*d*) normalized dissipation, buoyancy flux and production.

The wave amplitude is also found to affect the functional dependence of the flow on slope angle. When Fr is small, the critical case is laminar and there is turbulence only in a narrow range of near-critical angles. At high Fr, there is turbulence at all the slope angles considered here.

The mechanism of transition to turbulence is investigated. It is found that, during the initial transient when the amplitude of the density variation in the internal wave increases, regions of static instability ($Ri_g < 0$) as well as shear instability ($Ri_g < 0.25$) are formed. The gradient Richardson number is defined by $Ri_g = N^2/S^2$, where N represents the buoyancy frequency and S is shear defined by $S = \sqrt{(\mathrm{d}u_s/\mathrm{d}z_s)^2 + (\mathrm{d}v_s/\mathrm{d}z_s)^2}$ The present nonlinear simulations show that it is wave breaking by the convective instability just after flow reversal from downslope to upslope that leads to turbulence during critical slope reflection, similar to the result of Gayen & Sarkar (2011*a*) in the critical slope generation problem. In the case of near but not exactly critical reflection, transition to turbulence occurs at a different phase

and arises due to both shear instability in upslope flow ($Ri_g < 0.25$ owing to wave shear) as well as convective instability during flow reversal from upslope to downslope. The inviscid analytical solution of Scotti (2011) was evaluated in a near-critical case and shows regions with static and shear instability, thus providing guidance as to the formation of turbulence. However, quantitative predictions of turbulence require fully nonlinear simulations. For instance, the first region of static instability occurs earlier in the analytical solution than in the simulations and, at later time, the statically unstable regions in the analytical solution are substantially larger than the turbulence patches in the simulations.

After the initial transient, a reflected wave field is established with periodic flow that has quasi-steady amplitude and phase-dependent turbulence. The phasing of turbulence is examined when the off-criticality angle, $\alpha - \beta$, varies between 0 and 10°. There are important differences between critical and near-critical cases. When the slope is critical, there is a single prominent peak of TKE per cycle that occurs just after flow reversal from down- to upslope flow and is caused by positive buoyancy flux that occurs during the convective instability that accompanies the flow reversal event. The contribution of shear production to TKE is small. The phasing is similar when the off-criticality is 5°. In contrast, when the off-criticality has a larger value of 10°, turbulence is less regular and skips cycles. Both buoyancy flux and shear production are found to be important contributors to the TKE in the near-critical case. The results in the various cases are collected to quantify the parametric dependence of TKE and turbulent dissipation rate (averaged over time and over distance above bottom) on slope angle and Froude number. Interestingly, it is found that reflection at near-critical angles can lead to more intense turbulence than critical slope reflection, for waves with small amplitude, that is, small Fr. The reason for this low-Fr behaviour is that, although the velocity intensification is smaller when the slope is off-critical, the convectively unstable region, not being restrained by the boundary, can be larger and thereby lead to stronger turbulence than the exactly critical case. At higher Fr, the values of TKE and turbulent dissipation rate exhibit a monotonic decrease with increasing off-criticality.

At a given slope angle, the TKE and turbulent dissipation rate increase with increasing Fr. When normalized by incoming wave properties, the variability of turbulent statistics at high Fr decreases. In the present simulations, the maximum value of averaged TKE is approximately 7 % of the incoming wave kinetic energy, K_{wave}, and the maximum value of averaged dissipation rate is approximately 5 % of ΩK_{wave}. If turbulent statistics, when appropriately normalized by wave characteristics, saturate with increasing Fr, parameterizations of wave dissipation for use in ocean models will be facilitated. Nevertheless, more work is necessary to establish if the results found in the present simulations hold under more general parametric variation as well as at geophysical scales.

REFERENCES

AUCAN, J., MERRIFIELD, M. A., LUTHER, D. S. & FLAMENT, P. 2006 Tidal mixing events on the deep flanks of Kaena Ridge, Hawaii. *J. Phys. Oceanogr.* **36**, 1202–1219.

BLUTEAU, C. E., JONES, N. L. & IVEY, G. N. 2011 Dynamics of a tidally-forced stratified shear flow on the continental slope. *J. Geophys. Res.* **116**, C11017.

CACCHIONE, D. A., PRATSON, L. F. & OGSTON, A. S. 2002 The shaping of continental slopes by internal tides. *Science* **296**, 724–727.

DAUXOIS, T. & YOUNG, W. R. 1999 Near-critical reflection of internal waves. *J. Fluid Mech.* **390**, 271–295.

DESILVA, I. P. D., IMBERGER, J. & IVEY, G. N. 1997 Localized mixing due to a breaking internal wave ray at a sloping bed. *J. Fluid Mech.* **350**, 1–27.

ERIKSEN, C. C. 1998 Internal wave reflection and mixing at Fieberling Guyot. *J. Geophy. Res.* **103**, 2977–2994.

GAYEN, B. & SARKAR, S. 2010 Turbulence during the generation of internal tide on a critical slope. *Phys. Rev. Lett.* **104**, 218502.

GAYEN, B. & SARKAR, S. 2011*a* Boundary mixing by density overturns in an internal tidal beam. *Geophys. Res. Lett.* **38**, L14608.

GAYEN, B. & SARKAR, S. 2011*b* Negative turbulent production during flow reversal in a stratified oscillating boundary layer on a sloping bottom. *Phys. Fluids* **23**, 101703.

IVEY, G. N. & NOKES, R. I. 1989 Vertical mixing due to the breaking of critical internal waves on sloping boundaries. *J. Fluid Mech.* **204**, 479–500.

JAVAM, A., IMBERGER, J. & ARMFIELD, S. W. 1999 Numerical study of internal wave reflection from sloping boundaries. *J. Fluid Mech.* **396**, 183–201.

LAURENT, L. C. ST. & GARRETT, C. 2002 The role of internal tides in mixing the deep ocean. *J. Phys. Oceanogr.* **32**, 2882–2899.

LELE, S. 1992 Compact finite difference schemes with spectral like resolution. *J. Comput. Phys.* **103**, 16–42.

MOUM, J. N., CALDWELL, D. R., NASH, J. D. & GUNDERSON, G. D. 2002 Observations of boundary mixing over the continental slope. *J. Phys. Oceanogr.* **32**, 2113–2130.

MUNK, W. & WUNSCH, C. 1998 Abyssal recipes II: energetics of tidal and wind mixing. *Deep-Sea Res.* I **45**, 1977–2010.

NASH, J. D., KUNZE, E., TOOLE, J. M. & SCHMITT, R. W. 2004 Internal tide reflection and turbulent mixing on the continental slope. *J. Phys. Oceanogr.* **34**, 1117–1134.

PARK, Y.-G. & BRYAN, K. 2000 Comparison of thermally driven circulation from a depth-coordinate model and an isopycnal-layer model. Part I: scaling-law sensitivity to vertical diffusivity. *J. Phys. Oceanogr.* **30**, 590–605.

PHILLIPS, O. M. 1970 On flows induced by diffusion in a stably stratified fluid. *Deep-Sea Res.* **17**, 435–443.

PHILLIPS, O. M. 1977 *The Dynamics of the Upper Ocean*, 2nd edn. Cambridge University Press.

RODENBORN, B., KIEFER, D., ZHANG, H. P. & SWINNEY, H. L. 2011 Harmonic generation by reflecting internal waves. *Phys. Fluids* **23**, 026601.

SAENKO, O. A. 2005 The effect of localized mixing on the ocean circulation and time-dependent climate change. *J. Phys. Oceanogr.* **36**, 140–160.

SCOTTI, A. 2011 Inviscid critical and near-critical reflection of internal waves in the time domain. *J. Fluid Mech.* **674**, 464–488.

SLINN, D. N. & RILEY, J. J. 1998*a* A model for the simulation of turbulent boundary layers in an incompressible stratified flow. *J. Comput. Phys.* **34**, 550–602.

SLINN, D. N. & RILEY, J. J. 1998*b* Turbulent dynamics of a critically reflecting internal gravity wave. *Theor. Comput. Fluid Dyn.* **11**, 281–303.

TABAEI, A., AKYLAS, T. R. & LAMB, K. 2005 Nonlinear effects in reflecting and colliding internal wave beams. *J. Fluid Mech.* **526**, 217–243.

THORPE, S. A. 1987 On the reflection of a train of finite-amplitude internal waves from a uniform slope. *J. Fluid Mech.* **178**, 279–302.

THORPE, S. A. 1992 Thermal fronts caused by internal gravity waves reflecting from a slope. *J. Phys. Oceanogr.* **22**, 105–108.

VALLIS, G. K. 2000 Large-scale circulation and production of stratification: effects of wind, geometry, and diffusion. *J. Phys. Oceanogr.* **30**, 933–954.

WUNSCH, C. 1968 On the propagation of internal waves up a slope. *Deep-Sea Res.* **25**, 251–258.

WUNSCH, C. 1970 On oceanic boundary mixing. *Deep-Sea Res.* **17**, 293–301.

WUNSCH, C. & FERRARI, R. 2004 Vertical mixing, energy, and the general circulation of the oceans. *Annu. Rev. Fluid Mech.* **36**, 281–314.